Available online at www.sciencedirect.com
ScienceDirect
Comput. Methods Appl. Mech. Engrg. 349 (2019) 550–575
Computer methods in applied mechanics and engineering
www.elsevier.com/locate/cma

An adapting cohesive approach for crack-healing analysis in SMA fiber-reinforced composites

M. Karimi, H. Bayesteh, S. Mohammadi*

High Performance Computing Lab, School of Civil Engineering, College of Engineering, University of Tehran, Tehran, Iran

Received 30 June 2018; received in revised form 18 December 2018; accepted 15 February 2019
Available online 28 February 2019

Abstract

In this study, a varying/adapting cohesive approach is developed to model crack-healing procedure in reinforced shape memory composites. To this aim, the stress–strain behavior of SMA fiber in thermo-mechanical condition is converted into a traction–separation response between crack faces. The extended finite element formulation is employed to model crack in reinforced composites and to avoid remeshing while maintaining the required accuracy of results. Combination of XFEM to model arbitrary crack and traction–separation formulation enables the model to simulate mixed-mode crack propagation and crack-healing with different fiber orientations. Examining the results shows that the proposed model maintains the precision of direct modeling of SMA fibers while decreasing the computational costs and complexity of modeling significantly.

Keywords: Self-healing; Propagation; Shape memory alloy; Composite; Cohesive

1. Introduction

Shape memory alloys (SMAs) are among the most popular smart materials used in different applications such as: stents and self-expanding micro structures in biomedical engineering, morphing structures in aerospace industries, dampers in civil engineering applications and actuators in smart composite structures.

These materials can undergo large deformation and dissipate large amount of energy due to super elastic and shape memory effect behaviors. The super elastic behavior occurs when a loading–unloading stress cycle occurs at a fixed temperature value, allowing the material to return to its original shape. The shape memory effect occurs when SMA undergoes a loading–unloading stress cycle with some inelastic strain, while no reverse transformation occurs.

Active composites have recently been used in different areas, with many devoted researches to examine their behavior. Some micromechanical models, proposed to predict the thermo-mechanical response of unidirectional SMA composites [1–3], performed well, but with the cost of increased complexity of modeling.

Several numerical studies investigated SMA reinforced composite behavior by the finite element method [4–17]. For instance, Lagoudas et al. [4], Marfia et al. [5] and Bodaghi et al. [6] studied the thermo-mechanical response

* Corresponding author.
E-mail address: smoham@ut.ac.ir (S. Mohammadi).

https://doi.org/10.1016/j.cma.2019.02.019
0045-7825/

of SMA composites based on the laminate theory, and used the finite element method to simulate matrix and SMA layers. Some studies simulated SMA composites based on the laminate theory [7], and the classical plate theory [8], by the assumption that SMA wires were distributed uniformly in the matrix. Gomsheie et al. [9] introduced a nonlinear finite element method based on shear deformation theory to model SMA composites, with a perfect bond between the matrix and wires.

The thermal buckling behavior of SMA composites was investigated by Lee et al. [10] based on the linear buckling formulation, using the two-node elements for SMA wires and four-node shell elements for the matrix. Park et al. [11] studied the problem of composite plate with embedded SMA fibers using the first order shear deformation theory for investigation of influence of SMA fibers on thermal post-buckling deflection and frequency. Later, Marfia and Sacco [12] proposed a non-linear homogenization method to examine the buckling behavior of laminated SMA composites. Furthermore, a 3D hierarchical multiscale method has been recently presented by Fatemi et al. [13] to investigate the macroscopic and microscopic behavior of SMA fiber reinforced composites.

One of the potential SMA composite applications is in smart materials for crack repair or healing. Several experimental studies were dedicated to examine crack closure in SMA composites [18,19] and self-healing of metal matrix under tensile stress by SMA-wire reinforcement [20,21].

There are valuable studies to investigate the failure mechanism of fiber reinforced composites [22], namely the intralaminar damage model of progressive failure of composites by Riccio and coauthors in [23,24] based on energy balance and cohesive damage model. However, limited numerical studies on crack closure in SMA composites are available. Araki [25] used a micromechanical method to investigate the crack healing based on the stress intensify factor. The finite element method was adopted to simulate self-healing, and to model embedded fibers and matrix separately, with the assumption of either a poor or a perfect bond between reinforcement and matrix [26,27].

From numerical perspective, the extended finite element method (XFEM) method, usually adopted for simulating crack propagation in different static and dynamic problems [28–31], shear bands [32,33], multi field problems [34,35], dislocation [36], and cohesive crack simulations [37–39], has been extensively developed. In contrast to modeling crack growth with the finite element method, which requires remeshing when the crack extends into elements [40–42], the extended finite element method is capable of modeling arbitrary discontinuities without any remeshing [43], which facilitates the crack propagation simulations [38,39]. XFEM cohesive based models have also been increasingly used for modeling crack propagation in fiber composites; simulation of delamination in unidirectional reinforced composites [44,45], mode I fracture of unidirectional carbon/epoxy composites [46], and zigzag delamination under mode I loading [47]. Accordingly, XFEM is used as a robust method to crack simulation in this paper.

To the knowledge of the authors, this study presents the first simulation of crack-healing that does not need direct and separate modeling of embedded SMA fibers, matrix and their bonding. The proposed model decreases the computational complexity of direct models, especially for simulating composites with large number of SMA fibers. In addition, this method exceeds previous works in its ability to simulate crack propagation in SMA reinforced composites with different fiber orientations and its potential to simulate mixed-mode crack propagation and healing in various loading conditions.

In this work, a new approach is developed based on an adapting cohesive formulation to simulate general crack healing behavior in SMA-fiber composites. In the proposed model, based on the cohesive idea, the stress–strain of SMA fibers is converted to a traction–separation law and is lumped on the crack surfaces. During the loading, traction increases on the crack faces, which depends on the existence of bridging fibers, the crack direction and the crack opening. Due to the fact that fibers in different parts of crack experience different levels of stress and strain, therefore, values of martensitic volume fraction of fibers do not match; leading to a varying cohesive response along the crack path. In fact, the cohesive response adapts itself for different bridging fibers.

A schematic self-healing process in a cracked specimen is depicted in Fig. 1. Before the initiation of mechanical loading, fibers are stress and strain free (Fig. 1a). During the mechanical loading, the crack propagates, and the fibers begin to strengthen the specimen by the bridging effect (Fig. 1b). By increasing the temperature, the strain decreases due to the reverse phase transformation of fibers, leading to crack closure and healing (Fig. 1c).

The present study consists of the following discussions. Section 2 briefly demonstrates the shape memory alloy constitutive model, followed by presenting a direct model to simulate the healing process without crack propagation in Section 3. Then, the proposed adapting cohesive crack model is presented, which includes discussion on the extended finite element model, cohesive zone modeling and propagation algorithm. Section 4 verifies the model by solving benchmark bending, tension and mixed mode fracture problems, followed by necessary discussions. The concluding remarks are then provided in the conclusion section.

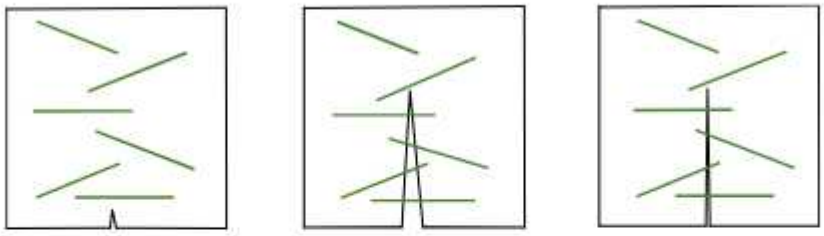

Fig. 1. Schematic crack-healing process due to thermomechanical loading (a) initial state, (b) mechanical loading (bridging fibers), (c) thermal loading (healing process).

2. SMA constitutive model

The constitutive model proposed by Boyd and Lagoudas [48] is used in this study. Accordingly, the total strain consists of two parts of thermo-elastic ε^{th} strain and inelastic ε^{in} strain:

$$\varepsilon = \varepsilon^{in} + \varepsilon^{th} \tag{1}$$

The inelastic strain generally includes two parts of the transformation strain ε^{t} and the plastic strain ε^{p}. The plastic strain is assumed negligible, and $\varepsilon^{in} = \varepsilon^{t}$ [49]. Accordingly, the Gibbs free energy, which is a function of independent variables of stress $\boldsymbol{\sigma}$ and temperature T, and the internal state variables of the martensitic volume fraction ξ and strain ε can be written as [49],

$$\begin{aligned} G(\boldsymbol{\sigma}, \mathrm{T}, \xi, \varepsilon) = & -\frac{1}{2\rho}\boldsymbol{\sigma} : \boldsymbol{S} : \boldsymbol{\sigma} - \frac{1}{\rho}\boldsymbol{\sigma} : [\boldsymbol{\alpha}(\mathrm{T} - \mathrm{T}_0) + \varepsilon] \\ & + c\left[(T - T_0) - \mathrm{T}\ln(\frac{T}{T_0})\right] - s_0 T + u_0 + \frac{1}{\rho} f(\xi) \end{aligned} \tag{2}$$

where c, s_0, u_0 and T_0 are the effective specific heat, the effective specific entropy, the effective specific internal energy and the reference temperature, respectively. In addition, $\boldsymbol{S}$ and $\boldsymbol{\alpha}$ are the effective compliance and the thermal expansion tensors, respectively. The effective material properties are determined from the martensitic volume fraction ξ [49]:

$$\boldsymbol{S}(\xi) = \boldsymbol{S}^{A} + \xi(\boldsymbol{S}^{M} - \boldsymbol{S}^{A}) \tag{3}$$

$$\boldsymbol{\alpha}(\xi) = \boldsymbol{\alpha}^{A} + \xi(\boldsymbol{\alpha}^{M} - \boldsymbol{\alpha}^{A}) \tag{4}$$

$$c(\xi) = c^{A} + \xi(c^{M} - c^{A}) \tag{5}$$

$$s_0(\xi) = s_0^{A} + \xi(s_0^{M} - s_0^{A}) \tag{6}$$

$$u_0(\xi) = u_0^{A} + \xi(u_0^{M} - u_0^{A}) \tag{7}$$

where A and M represent the austenitic and martensitic phases, respectively.

The transformation strain and martensitic volume fraction during the forward and reverse transformations are related as [49]

$$\dot{\varepsilon} = \boldsymbol{\Lambda}\dot{\xi} \tag{8}$$

where $\boldsymbol{\Lambda}$ is the transformation tensor,

$$\boldsymbol{\Lambda} = \begin{cases} \dfrac{3}{2}\varepsilon^{\max}\dfrac{\boldsymbol{\sigma}'}{\overline{\sigma}'} & \dot{\xi} > 0 \\ \varepsilon^{\max}\dfrac{\varepsilon^{t-r}}{\overline{\varepsilon}^{t-r}} & \dot{\xi} < 0 \end{cases} \tag{9}$$

with

$$\overline{\sigma}' = \sqrt{\frac{3}{2}\|\boldsymbol{\sigma}'\|^2} \tag{10}$$

$$\bar{\varepsilon}^{t-r} = \sqrt{\frac{2}{3}\|\varepsilon^{t-r}\|^2} \tag{11}$$

$\varepsilon^{\max}$ is the maximum transformation strain, $\boldsymbol{\sigma}'$ is the deviatoric stress tensor, and ε^{t-r} represents the transformation strain at the reversal point ($\xi = 1$ for the martensite reversal point, and $\xi = 0$ for the austenite reversal point).

Using the second law of thermodynamics, Eq. (8) can be written in the following form [49]

$$\left(\boldsymbol{\sigma} : \boldsymbol{\Lambda} - \rho\frac{\partial G}{\partial \xi}\right)\dot{\xi} = \pi\dot{\xi} \geq 0 \tag{12}$$

where π is determined from $\boldsymbol{\sigma}$, T and ξ [49],

$$\begin{aligned}\pi(\boldsymbol{\sigma}, T, \xi) = {} & \boldsymbol{\sigma} : \boldsymbol{\Lambda} + \frac{1}{2}\boldsymbol{\sigma} : \Delta\boldsymbol{S} : \boldsymbol{\sigma} + \boldsymbol{\sigma} : \Delta\boldsymbol{\alpha}(T - T_0) \\ & -\rho\Delta c\left[(T - T_0) - T\ln\left(\frac{T}{T_0}\right)\right] + \rho\Delta s_0 T - \rho\Delta u_0 - \frac{\partial f}{\partial \xi}\end{aligned} \tag{13}$$

f is the hardening function, defined by Eq. (14) based on the Boyd and Lagoudas [48] model

$$f(\xi) = \begin{cases} \frac{1}{2}\rho b^M \xi^2 + (\mu_1 + \mu_2)\xi & \dot{\xi} > 0 \\ \frac{1}{2}\rho b^A \xi^2 + (\mu_1 - \mu_2)\xi & \dot{\xi} < 0 \end{cases} \tag{14}$$

where b^A, b^M, μ_1 and μ_2 are the model parameters

$$\begin{aligned} b^M &= -\Delta s_0(\mathrm{T}_s^M - \mathrm{T}_f^M) \\ b^A &= -\Delta s_0(\mathrm{T}_f^A - \mathrm{T}_s^A) \\ \mu_1 &= \frac{1}{2}\rho\Delta s_0(\mathrm{T}_s^M + \mathrm{T}_f^A) - \rho\Delta u_0 \\ \mu_2 &= \frac{1}{4}\rho\Delta s_0(\mathrm{T}_s^A + \mathrm{T}_s^M - \mathrm{T}_f^A - \mathrm{T}_f^M) - \rho\Delta u_0 \\ Y &= \frac{1}{4}\rho\Delta s_0(\mathrm{T}_f^M + \mathrm{T}_s^M - \mathrm{T}_f^A - \mathrm{T}_s^A) \end{aligned} \tag{15}$$

$\dot{\xi}$ is assumed positive during the forward martensitic transformation. As a result, π must have a positive value in the forward martensite transformation, while it becomes negative during the reverse martensitic transformation. When no phase transformation is taking place, $\dot{\xi} = 0$ and Eq. (12) remains satisfied. These processes are defined by the following transformation function Φ [49],

$$\Phi = \begin{cases} \pi - Y & \dot{\xi} > 0 \quad (A \to M) \\ -\pi - Y & \dot{\xi} < 0 \quad (\mathrm{M} \to A) \end{cases} \tag{16}$$

In this study, a one-dimensional constitutive model based on the key variables of temperature T and total strain ε is employed for SMA fibers. Before initiating the loading process, fibers are in the fully austenitic phase, and the martensitic volume fraction is zero, $\xi = 0$. During the loading and heating, deformation and stress of the specimen are updated in each step. In addition, the martensitic volume fraction ξ is updated in each step to capture the forward and reverse transformations.

For the forward phase transformation under the mechanical loading, Eq. (16) can be solved for ξ as [49]

$$\xi = \frac{1}{\rho b^M}\left[|\boldsymbol{\sigma}|\,\varepsilon^{\max} + \frac{1}{2}\Delta\boldsymbol{S}\boldsymbol{\sigma}^2 + \rho\Delta s_0(T - T_s^M)\right] \tag{17}$$

After initiation of thermal loading, fibers initially behave elastically. When the temperature is between T_s^A and T_f^A ($T_s^A < T \leq T_f^A$) the reverse phase transformation occurs, and Eq. (16) can be solved for ξ as [49]

$$\xi = \frac{1}{\rho b^A}\left[|\boldsymbol{\sigma}|\,\varepsilon^{\max} + \frac{1}{2}\Delta\boldsymbol{S}\boldsymbol{\sigma}^2 + \rho\Delta s_0(T - T_f^A)\right] \tag{18}$$

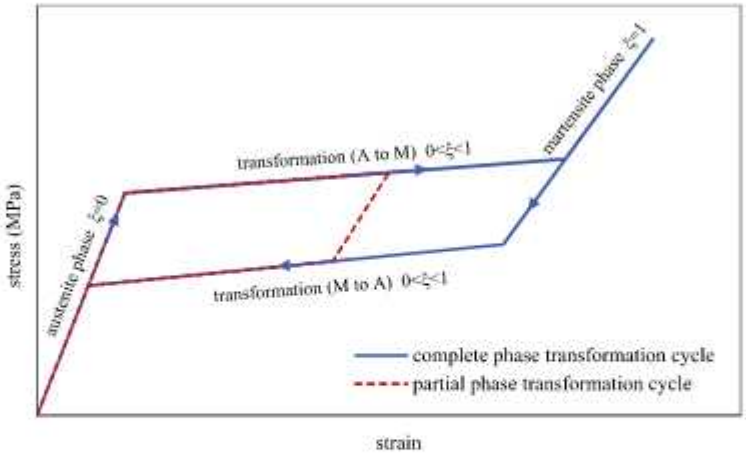

Fig. 2. Typical forward and reverse transformation paths.

Substituting Eq. (16) into the one-dimensional form of total strain (Eq. (19)), the total strain for the forward and reverse phase transformations can be written as [49]

$$\varepsilon = \boldsymbol{S}(\xi)\boldsymbol{\sigma} + \boldsymbol{\alpha}(\xi)(T - T_0) + \varepsilon^t \tag{19}$$

$$\varepsilon = \boldsymbol{S}(\xi)\boldsymbol{\sigma} + \boldsymbol{\alpha}(\xi)(T - T_0) + \varepsilon^{\max}\mathrm{sgn}(\sigma)\xi \tag{20}$$

Based on the phase transformation function Φ (Eq. (16)), the forward phase transformation occurs when [49]:

$$\Phi = 0 \Rightarrow \pi = Y \tag{21}$$

Substituting $\xi = 0$ in Eq. (21), leads to a relation between $\boldsymbol{\sigma}$ and T, which represent the beginning of forward phase transformation in different temperatures. The following nonlinear relations describe the equation of colored lines in Fig. 3.

(i) Initiation of forward phase transformation: $\pi = Y, \xi = 0$
(ii) End of forward phase transformation: $\pi = Y, \xi = 1$
(iii) Initiation of reverse phase transformation: $\pi = -Y, \xi = 1$
(iv) End of reverse phase transformation: $\pi = -Y, \xi = 0$

At the end of loading part, each fiber has a martensitic volume fraction, which depends on their corresponding loading condition. Therefore, each fiber has a different stress–strain path, which depends on the geometry of fibers and the undergoing strain. As a result, some fibers experience a complete cycle of forward and reverse phase transformation, while the others may experience only a partial phase transformation cycle. Fig. 2 represents the typical complete and partial cycles of forward and reverse phase transformation paths for a fiber. Fibers that undergo a lower level of stress and experience a partial cycle of forward phase transformation have lower T_s^A; their reverse phase transformations initiate sooner (Fig. 3).

Fig. 3 shows a typical loading/heating path for an SMA fiber in a composite. The loading starts with an initial high temperature (point 1) when the fiber is in the fully austenite phase and continues up to point (2). Increasing the load at the same temperature leads to the forward phase transformation between σ_s^M (point 2) and σ_f^M (point 3). The heating part initiates at point (4) with a little decrease in stress due to the increase of temperature under a steady external loading. When the stress in fiber reaches σ_s^A, the reverse transformation starts at point (5), causing a decrease of strain in the fiber and a complete shape recovery by point (6) (as a result of stress increase). After completing the reverse phase transformation, heating causes an increase in the fiber strain, which leads to a decrease in the stress level.

3. Cohesive model of healing process

The objective of this paper is to present an effective method for simulation of healing process of SMA composites based on adapting cohesive crack idea. To this aim, a specific length near the crack faces for each fiber is assumed

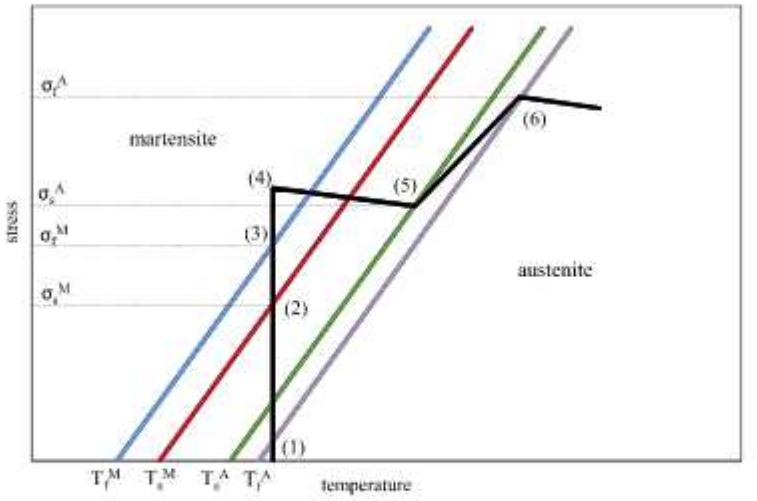

Fig. 3. Typical loading and heating paths; s and f represent start and finish points of phase transformation.

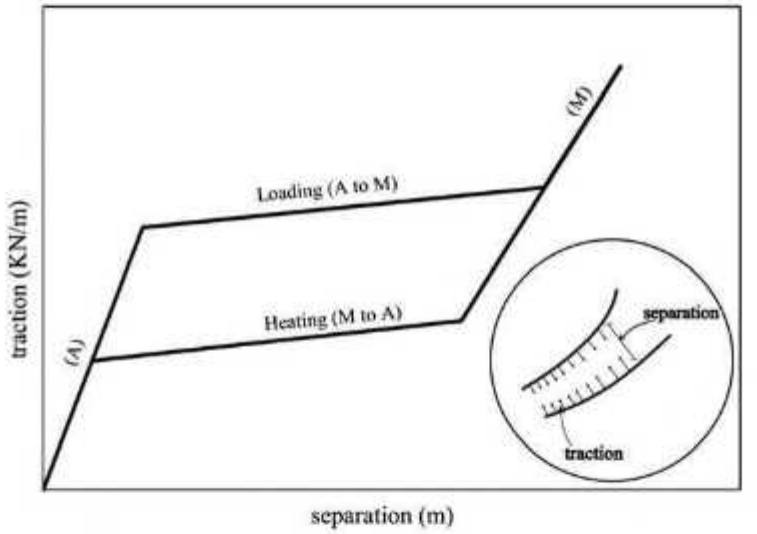

Fig. 4. Typical traction–separation law obtained from the SMA stress–strain response.

to represent the local debonding between fibers and matrix. A traction–separation law is then derived from the stress–strain response of SMA fiber to determine the traction acting from fibers on the crack edges. Fig. 4 depicts such a typical SMA-based traction–separation law, where the separation is computed from the fiber deformation along the local debonding length. Fibers bridging different parts of the crack undergo different levels of stress, strain and martensitic volume fraction. As a result, an adapting traction–separation law will be obtained for each fiber.

In the loading process, deformation, crack opening and traction on the crack faces are updated in each step. During the heating process, increase of temperature causes the reverse transformation in remaining fibers, which generates sufficient normal traction on the crack faces for crack closure.

3.1. XFEM displacement field

To better capture the healing process of cohesive crack in SMA composites, the well-known XFEM formulation is adopted. The displacement field $\boldsymbol{u}$ consists of the classical $\boldsymbol{u}^{FEM}$ and the crack-slip $\boldsymbol{u}^{H}$ displacements,

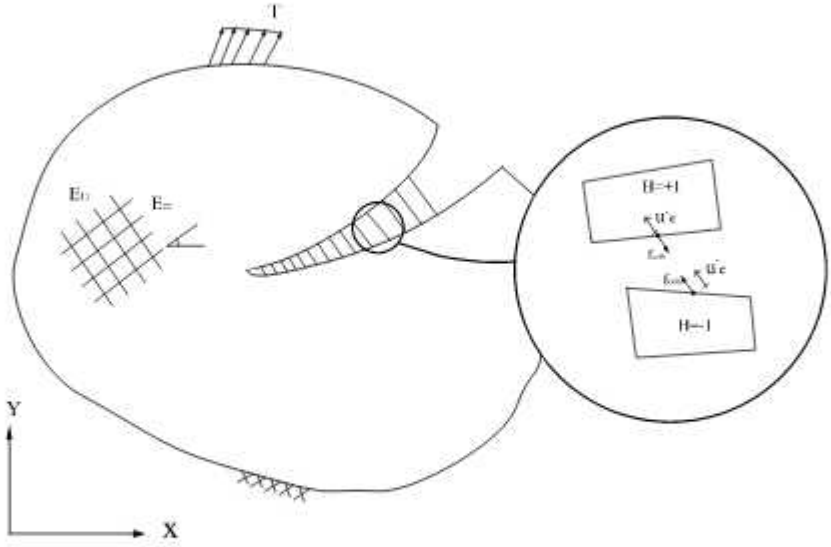

Fig. 5. A typical fiber bridging the crack and definition of $\bar{u}_e$.

respectively [28]:

$$\boldsymbol{u}^{XFEM}(x) = \boldsymbol{u}^{FEM}(x) + \boldsymbol{u}^{H}(x) \tag{22}$$

$$\boldsymbol{u}^{XFEM}(x) = \left[\sum_j N_j(x)\boldsymbol{u}_j\right] + \left[\sum_j N_j(x)H(x)\boldsymbol{a}_j\right] \tag{23}$$

N is the standard finite element shape function, and H is the Heaviside function, representing the crack discontinuous displacement field

$$H(x) = \begin{cases} +1 & (x - x^*).\boldsymbol{n}_c > 0 \\ -1 & (x - x^*).\boldsymbol{n}_c < 0 \end{cases} \tag{24}$$

where x^* is the projection of x on crack line and $\boldsymbol{n}_c$ represents the normal vector of crack at point x^*.

3.2. Cohesive formulation

In order to determine the traction on crack faces, an idea similar to spring elements between the crack edges is assumed, as depicted in Fig. 5.

Crack opening along the fiber direction can be determined from [38],

$$\bar{u}_e = \boldsymbol{u}_e^+ - \boldsymbol{u}_e^- \tag{25}$$

$$\boldsymbol{u}_e^+ = \sum_i \left(N_i\boldsymbol{u}_i + N_i(1 - H)\boldsymbol{a}_i\right).\boldsymbol{e}_{bar} \tag{26}$$

$$\boldsymbol{u}_e^- = \sum_i \left(N_i\boldsymbol{u}_i + N_i(-1 - H)\boldsymbol{a}_i\right).\boldsymbol{e}_{bar} \tag{27}$$

where $\boldsymbol{e}_{bar}$ is the unit vector along the fiber direction. This approach allows for crack propagation in composites with different fiber directions. Traction of crack surfaces $\boldsymbol{\tau}^c$ can be determined from the typical cohesive law of Fig. 4.

The equilibrium equation can be written as

$$\boldsymbol{f}_{ext} - \boldsymbol{f}_{int} - \boldsymbol{f}_{coh} = 0 \tag{28}$$

where $\boldsymbol{f}_{ext}$, $\boldsymbol{f}_{int}$, and $\boldsymbol{f}_{coh}$ are the external, internal and cohesive force vectors, respectively.

The force vectors can be written in terms of the standard and enrichment parts:

$$\boldsymbol{f}_{\text{int}} = \boldsymbol{f}_{\text{int}}^{sta} + \boldsymbol{f}_{\text{int}}^{enr} \tag{29}$$

$$\boldsymbol{f}_{ext} = \boldsymbol{f}_{ext}^{sta} + \boldsymbol{f}_{ext}^{enr} \tag{30}$$

where

$$\begin{aligned} \boldsymbol{f}_{\text{int}}^{sta} &= \int_{\Omega} \left(\boldsymbol{B}_i^u\right)^T \boldsymbol{\sigma} d\Omega \\ \boldsymbol{f}_{\text{int}}^{enr} &= \int_{\Omega} \left(\boldsymbol{B}_i^a\right)^T \boldsymbol{\sigma} d\Omega \end{aligned} \tag{31}$$

$$\begin{aligned} \boldsymbol{f}_{ext}^{sta} &= \int_{\Gamma_T} \boldsymbol{N}_i \boldsymbol{T} d\Gamma_T + \int_{\Omega} \boldsymbol{N}_i \boldsymbol{b} d\Omega \\ \boldsymbol{f}_{ext}^{enr} &= \int_{\Gamma_T} \boldsymbol{N}_i \psi_i \boldsymbol{T} d\Gamma_T + \int_{\Omega} \boldsymbol{N}_i \psi_i \boldsymbol{b} d\Omega \end{aligned} \tag{32}$$

Ω is the domain which consists of the cohesive interface and Γ_T is the traction boundary. $\boldsymbol{b}$ and $\boldsymbol{T}$ are body force and external traction vectors, respectively. Here, $\boldsymbol{N}$ is the standard finite element shape function and ψ is the enrichment function.

The cohesive force vector can similarly be defined

$$\boldsymbol{f}_{coh} = \boldsymbol{f}_{coh}^{sta} + \boldsymbol{f}_{coh}^{enr} \tag{33}$$

The cohesive formulation requires equivalent tractions on the opposite face of crack ($\boldsymbol{\tau}^{c+}$ and $\boldsymbol{\tau}^{c-}$ represent the traction of upper and lower crack faces, respectively),

$$\boldsymbol{\tau}^c = \boldsymbol{\tau}^{c+} = -\boldsymbol{\tau}^{c-} \tag{34}$$

that leads to $\boldsymbol{f}_{coh}^{sta} = 0$ as

$$\boldsymbol{f}_{coh}^{sta} = \int_{\Gamma_e^{c+}} \boldsymbol{N}_i \boldsymbol{\tau}^{c+} d\Gamma_e^{c+} + \int_{\Gamma_e^{c-}} \boldsymbol{N}_i \boldsymbol{\tau}^{c-} d\Gamma_e^{c-} = 0 \tag{35}$$

$$\begin{aligned} \boldsymbol{f}_{coh}^{enr} &= \int_{\Gamma_e^{c+}} \boldsymbol{N}_i \left(1 - \mathrm{H}_i\right) \boldsymbol{a}_i . \boldsymbol{\tau}^{c+} d\Gamma_e^{c+} + \int_{\Gamma_e^{c-}} \boldsymbol{N}_i \left(-1 - \mathrm{H}_i\right) \boldsymbol{a}_i . \boldsymbol{\tau}^{c-} d\Gamma_e^{c-} = \\ & 2 \int_{\Gamma_e^c} \boldsymbol{N}_i \boldsymbol{a}_i . \boldsymbol{\tau}^c d\Gamma_e^c = \int_{\Gamma_e^c} \boldsymbol{M}_i^{fib} \boldsymbol{\tau}^c d\Gamma_e^c \end{aligned} \tag{36}$$

where $\boldsymbol{M}_i^{fib}$ is the global shape function of equivalent spring element in the global coordinate, which can be defined in terms of the fiber direction $\boldsymbol{e}_{fib}$ and the shape function $\boldsymbol{N}_i$ at the corresponding Gauss point

$$\boldsymbol{M}_i^{fib} = \left[2\boldsymbol{N}_i \boldsymbol{e}_{fib}.\boldsymbol{e}_X \;\; 2\boldsymbol{N}_i \boldsymbol{e}_{fib}.\boldsymbol{e}_Y\right] \tag{37}$$

Γ^{c+} and Γ^{c-} denote the upper and lower crack faces, respectively, Γ^c is the crack path, and $\boldsymbol{e}_X$ and $\boldsymbol{e}_Y$ represent the global directions.

For each cracked element e, the stiffness matrix can be computed from

$$\boldsymbol{K}_e = \begin{bmatrix} \boldsymbol{K}_{uu} & \boldsymbol{K}_{ua} \\ \boldsymbol{K}_{au} & \boldsymbol{K}_{aa} + \boldsymbol{K}_{coh} \end{bmatrix} \tag{38}$$

where the subscripts u and a represent the standard and enriched degree of freedoms, respectively, and $\boldsymbol{K}_{coh}$ is associated with the Heaviside enrichment degrees of freedom [50].

$$\boldsymbol{K}_{coh} = \int_{\Gamma^c} \left(\boldsymbol{M}_i^{fib}\right)^T k_i \left(\boldsymbol{M}_i^{fib}\right) d\Gamma^c \tag{39}$$

where k_i is the stiffness of equivalent spring element, based on Eq. (40).

$$k_i = \frac{E_i A_i}{L_d} \tag{40}$$

E_i is the modulus of equivalent spring element, and A_i and L_d are the equivalent cross section area of fibers in the split element and the debonding length, respectively.

Table 1
The developed adapting cohesive Algorithm.

(1) Given the initial material properties and initial loading values $F = F + \Delta F$, $T = T + \Delta T$, Compute the initial stiffness $\boldsymbol{K}_i$, and the external force $\boldsymbol{f}_i^{ext}$

(2) Compute $\Delta \boldsymbol{u}_i$ using $\boldsymbol{f}_i^{ext} = \boldsymbol{K}_i \Delta \boldsymbol{u}_i$, and update $\boldsymbol{u}_i$ with $\boldsymbol{u}_i = \boldsymbol{u}_{i-1} + \Delta \boldsymbol{u}_i$

(3) Given $\boldsymbol{u}_i$, compute $\boldsymbol{f}_i^{\text{int}}$ based on Eq. (31)

(4) Given $\boldsymbol{u}_i$, compute $\boldsymbol{f}_i^{coh}$ based on Table (2)

(5) Compute $\boldsymbol{K}_{coh}$ based on Eq. (39), update $\boldsymbol{K}_i$

(6) Compute the residual force $\boldsymbol{r}_i = \boldsymbol{f}_i^{ext} - \boldsymbol{f}_i^{\text{int}} - \boldsymbol{f}_i^{coh}$

(7) Check the convergence criterion $\|\boldsymbol{r}_i\| < tol$.

IF NO.

Solve $\boldsymbol{r}_i = \boldsymbol{K}_i \Delta \boldsymbol{u}_i$ for $\Delta \boldsymbol{u}_i$, go to step (3)

ELSE

Check crack propagation criterion

IF $G \geq G_{cr}$

update the crack geometry

go to step (3)

ELSE $(G < G_{cr})$

update the external load $F = F + \Delta F$, and the temperature $T = T + \Delta T$

go to step (2)

ENDIF

ENDIF

For solving the equilibrium equation (28), the iterative Newton–Raphson method is adopted. Tables 1 and 2 illustrate the algorithm of adapting cohesive method.

3.3. Crack propagation criterion

In this study, the energy release rate G is calculated in each step and compared with the critical energy release rate of material (G_{cr}) to determine the state of crack propagation. This is achieved by the equivalent domain J integral [38],

$$G = J = \int_A \left[\sigma_{ij} u_{i,1} - w\delta_{1j}\right] q_{,j} dA + \int_{\Gamma^{c+} \cup \Gamma^{c-}} \left[w\delta_{1j} - \sigma_{ij} u_{i,1}\right] q n_j ds$$
$$w = \frac{1}{2}\sigma_{ij} u_{ij} \tag{41}$$

Table 2
Algorithm for the developed adapting traction–separation law for crack-healing.

(1) Given $\boldsymbol{u}_i^e$ and T , compute ε_i^e

(2) Update σ_s^M , σ_f^M , σ_s^A , and σ_f^A based on Eq. (16)

(3) Update T_s^M , T_f^M , T_s^A , and T_f^A based on Eq. (16)

(4) Compute $\boldsymbol{\tau}_i^c$, based on the traction-separation diagram **Fig. 4**

(5) Compute ξ_i , based on Eq. (17) and Eq. (18)

IF mechanical loading

$$\begin{cases} \boldsymbol{\tau}_i^c \geq \sigma_f^M \rightarrow \xi_i = 1 \\ \sigma_s^M \leq \boldsymbol{\tau}_i^c < \sigma_f^M \rightarrow \xi_i = \dfrac{1}{\rho b^M}\left[\left|\boldsymbol{\tau}_i^c\right|\varepsilon^{\max} + \dfrac{1}{2}\Delta \boldsymbol{S}(\boldsymbol{\tau}_i^c)^2 + \rho \Delta s_0 (T - T_s^M)\right] \\ \boldsymbol{\tau}_i^c < \sigma_s^M \rightarrow \xi_i = 0 \end{cases}$$

ELSE (heating)

$$\begin{cases} T > T_f^A \rightarrow \xi_i = 1 \\ T_s^A < T \leq T_f^A \rightarrow \xi_i = \dfrac{1}{\rho b^A}\left[\left|\boldsymbol{\tau}_i^c\right|\varepsilon^{\max} + \dfrac{1}{2}\Delta \boldsymbol{S}(\boldsymbol{\tau}_i^c)^2 + \rho \Delta s_0 (T - T_f^A)\right] \\ T \leq T_s^A \rightarrow \xi_i = 0 \end{cases}$$

Compute $\Delta\varepsilon_i = \boldsymbol{\alpha}(\xi)(T - T_0) + \varepsilon^{\max}\,\mathrm{sgn}(\boldsymbol{\tau}_i^c)\xi$ (Eq. (20))

Compute $\varepsilon_i = \varepsilon_i^e - \Delta\varepsilon_i$

Update $\boldsymbol{\tau}_i^c$ based on $\varepsilon_i = \boldsymbol{\tau}_i^c \times \boldsymbol{S}_i$

ENDIF

(6) Compute $\boldsymbol{f}_i^{coh}$ based on Eq. (36)

where A is the area inside the J contour. The crack propagation direction is calculated by the maximum hoop stress criterion. Accordingly, the angle of crack propagation θ is obtained by [51],

$$\frac{K_I}{K_{Icr}}\cos^3\left(\frac{\theta}{2}\right) - \frac{3}{2}\frac{K_{II}}{K_{Icr}}\cos\left(\frac{\theta}{2}\right)\sin(\theta) = 1 \tag{42}$$

where K_I and K_{II} are the mode I and mode II stress intensify factors, respectively, which are calculated by solving the following equations, based on the auxiliary fields of the interaction integral approach [28],

$$\begin{aligned} M &= \int_A \left\{\sigma_{ij}u_{i,1}^{aux} + \sigma_{ij}^{aux}u_{i,1} - w^M\delta_{1j}\right\}q_{,j} + \int_{\Gamma^{c+}\cup\Gamma^{c-}}\left[w\delta_{1j} - \sigma_{ij}u_{i,1}^{aux} - \sigma_{ij}^{aux}u_{i,1}\right]qn_j ds \\ w^M &= \frac{1}{2}\left(\sigma_{ij}\varepsilon_{ij}^{aux} + \sigma_{ij}^{aux}\varepsilon_{ij}\right) \end{aligned} \tag{43}$$

Table 3
Material properties of shape memory alloy [49].

Property	Value
Martensite elastic modulus, E^M (MPa)	55 000
Astenite elastic modulus, E^A (MPa)	46 000
Thermal expansion coefficient, $\alpha^{M,A}$ (1/k)	22×10^{-6}
Maximum transformation strain, ε^{max}	0.056
Maximum strain	0.08
Poisson's ratio, $\upsilon^{M,A}$	0.33
Stress influence coefficient, $C^{M,A}$ (MPa/k)	7.4
Martensite start temperature, T_s^M (K)	245
Martensite finish temperature, T_f^M (K)	230
Astenite start temperature, T_s^A (K)	270
Astenite finish temperature, T_f^A (K)	280

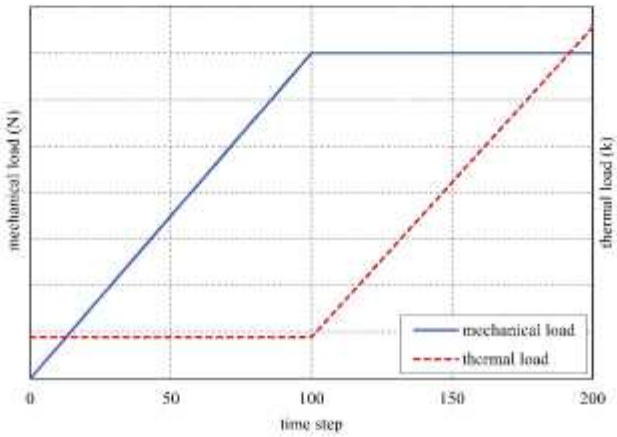

Fig. 6. Typical mechanical/thermal loading variations.

where the auxiliary fields u^{aux}, σ^{aux} and ε^{aux} are obtained from reference [51]. K_I and K_{II} can be computed from M according to

$$M = \frac{2}{E'}\left(K_I K_I^{aux} + K_{II} K_{II}^{aux}\right) \tag{44}$$

$$\begin{aligned} &\text{For mode I: } K_I^{aux} = 1,\ K_{II}^{aux} = 0 \\ &\text{For mode II: } K_I^{aux} = 0,\ K_{II}^{aux} = 1 \end{aligned} \tag{45}$$

4. Numerical simulations

In this section, first the developed cohesive extended finite element method is validated by a direct model that explicitly includes all SMA wires. The composite model consists of a brittle matrix and shape memory alloy wires, with properties defined in Table 3. A uniform heat change in fibers is considered during the healing process and the heat transfer between the matrix and fibers is neglected.

Fig. 6 depicts the mechanical/thermal loading process used for the analysis. A pseudo-time step is considered to define the mechanical/thermal loading process. At the first 100 time steps, the mechanical loading is increased and the temperature remains steady. Then, during the second part of analysis, the mechanical loading is kept steady and the temperature is increased. SMA fibers are assumed stress and strain free before applying the mechanical loads.

4.1. Direct modeling of the healing process

A model containing SMA fibers is adopted to verify the accuracy of the cohesive model. The matrix elements are modeled by standard 4-node elements, and SMA fibers are stimulated by embedded truss elements, whose stiffness

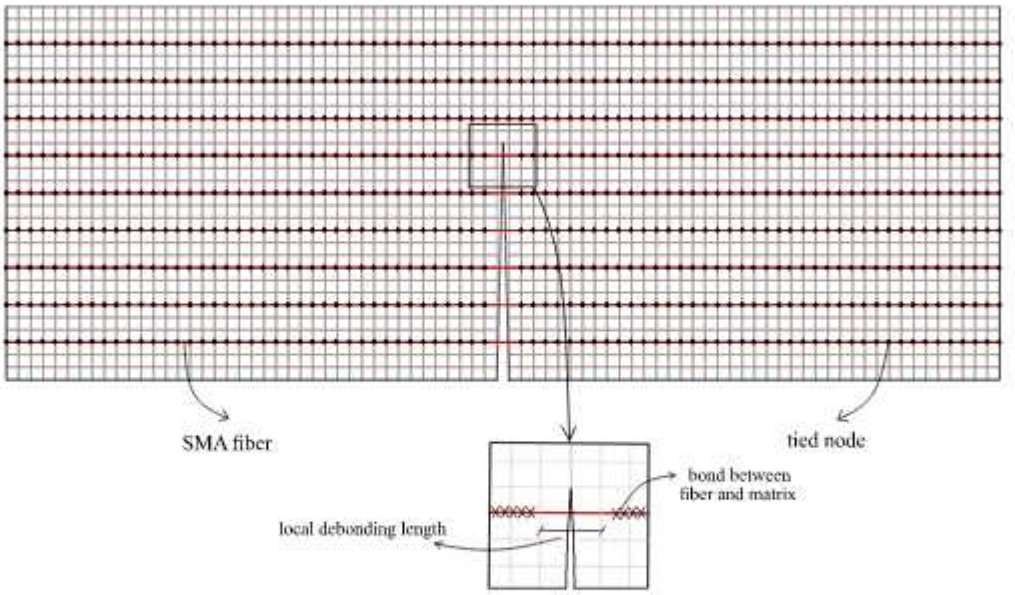

Fig. 7. Direct numerical modeling of SMA fibers with tied nodes and schematic presentation of fiber bridging.

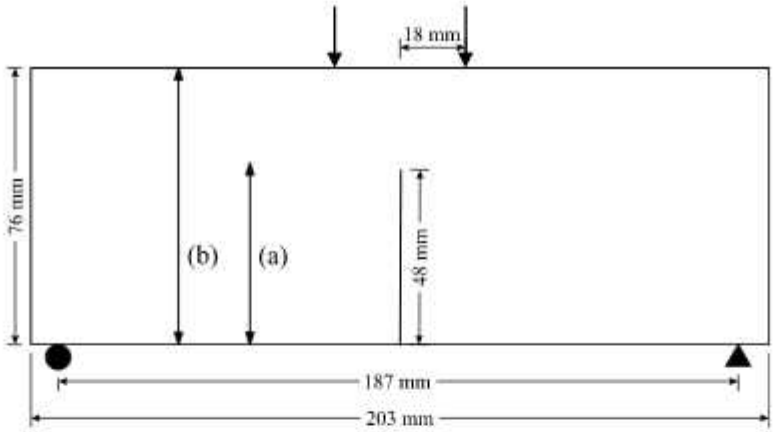

Fig. 8. Four-point bending beam, (a) and (b) represent the location interval of fibers for isotropic and orthotropic problems, respectively.

is added directly to the stiffness of matrix elements. In this model, fibers are tied to the matrix along the length of the fiber, except for a specific length (L_d) near the crack edges, where no connection is assumed (Fig. 7). This length is assumed to represent the local debonding zone for each fiber.

4.2. Four-point bending problem

In the first example, a four-point bending problem with SMA fibers, which are perpendicular to the initial crack, is considered. The configuration is depicted in Fig. 8 and the matrix properties are described in Table 4. The same Q4 mesh configuration of Fig. 7 is used without any truss elements (since the proposed method does not need any direct modeling of SMA fibers). No crack propagation analysis is performed in this example. The analysis is repeated for several local debonding lengths (L_d = 2.5, 7.5 and 17.5 mm) and under the same mechanical and thermal condition.

Table 4
Material properties of matrix.

Property	Value
Elastic modulus, E (MPa)	1300
Poisson's ratio, υ	0.21

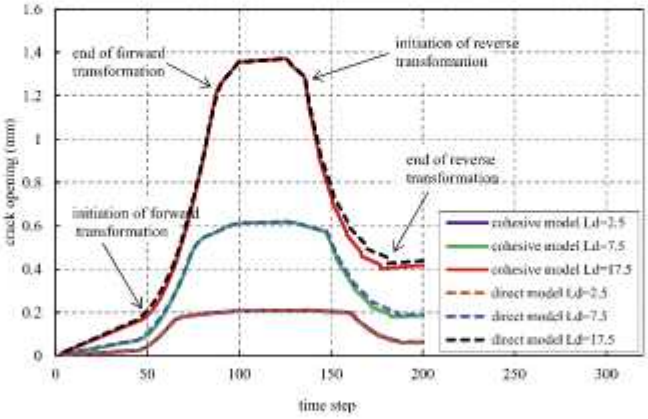

Fig. 9. Variations of crack opening in time for various fiber lengths L_d.

The analysis is performed in the plane strain state, with a force control condition. Each of the SMA fibers has a cross section of 2 mm^2, which represents a wire with 1.6 mm diameter (Volume fraction = 2%). A structured mesh of 2430 elements is used to model the beam.

4.2.1. Isotropic matrix

In this part, the matrix is considered isotropic with 9 fibers positioned across the length (a) of Fig. 8. The bond between matrix and fibers is neglected except at the end point of fibers [26]. For this purpose, in the direct model, the local debonding length is assumed equal to the total length of fibers ($L = L_d$). The four-point bending beam is analyzed under the point loading of 7000 N, with the initial temperature of 320 K, and the temperature increases to 470 K at the end of heating part. Variations of the maximum crack opening in time step during the mechanical/thermal loading processes, predicted by the direct and present cohesive models, are compared in Fig. 9. The first part of the diagram (first 100 time steps) shows the results of loading process for 3 different local debonding lengths of fibers before initiation, during and after completing the phase transformation.

The second part of diagram (second 100 time steps) shows the heating process that starts with a flat line from the end of loading part to the beginning of the reverse phase transformation. It shows little increase in crack opening due to the heating, but when the reverse phase transformation initiates, the fiber length decrease due to reverse phase transformation causes approximately 70 percent of crack closure.

Fig. 10 displays variations of the traction–crack opening, at the middle of the lowest cracked element, for both the direct and proposed cohesive models. Fibers in different positions show different stress–strain responses. The mechanical loading (first 100 time steps) causes increases in both traction and opening in each fiber. Initiation of the heating part (second 100 time steps) leads to little increase of traction and opening due to the increase in fibers temperature. The results show a gradual decreasing trend in the opening level by initiation of the reverse phase transformation of the fibers near the crack tip (Fig. 11). Near the crack tip fibers undergo lower level of stress and strain, therefore, have lower austenite start temperature. As a result, the reverse phase transformation initiates sooner near the crack tip. Due to the initiation of reverse phase transformation of each fiber near the crack tip, the strain level and the crack opening decrease. Consequently, the stress level increases near the crack tip while a decreasing trend is observed for the stress and strain in fibers far from the crack tip. This decreasing trend is clearly depicted between points A and B in Fig. 10. Then, by increasing the temperature gradually, the reverse phase transformation initiates in fibers far from the crack tip and the crack opening of the beam decreases significantly.

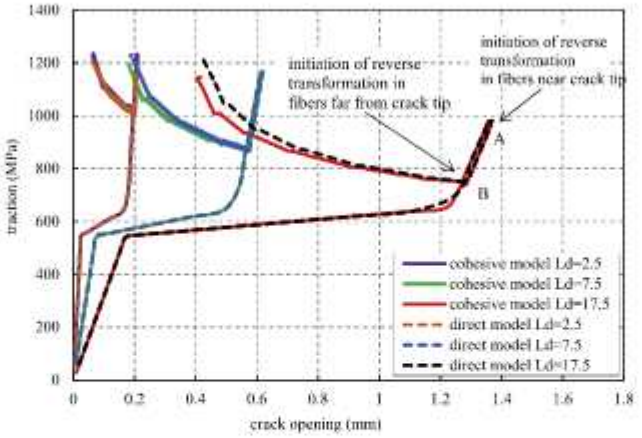

Fig. 10. Maximum traction–crack opening curves for various debonding lengths.

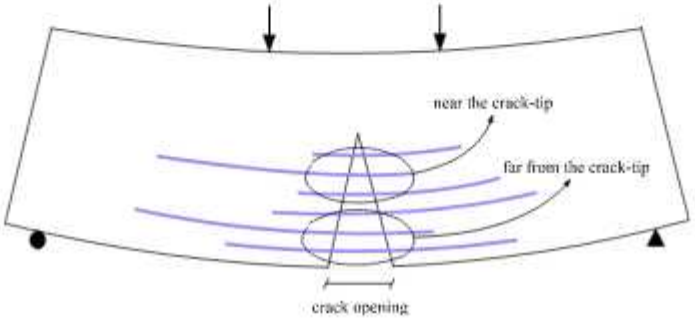

Fig. 11. Deformed bending beam.

Table 5
Error of crack opening for different local debonding lengths at the final step.

Local debonding length	Error
17.5 mm	4.8%
7.5 mm	2.5%
2.5 mm	0.05%

Figs. 9 and 10 show a good agreement between the proposed cohesive model and the direct approach for different fiber lengths. As depicted in these figures, clearly, the proposed method shows lower levels of error for shorter debonding lengths. This is due to the adopted assumption that most of deformation of SMA fibers is lumped in the cracked region. This assumption is more accurate for shorter debonding length, as clearly seen in Table 5 for the error of crack opening between the direct and adapting cohesive models for different local debonding lengths at the final step.

4.2.2. Orthotropic matrix

In this part, the matrix is assumed orthotropic with 14 fibers positioned across the length (b) of Fig. 8. In a direct model, this is achieved by tying each fiber to its corresponding matrix nodes along the fiber except for the debonding length. Equivalent properties of the cohesive model are obtained from the orthotropic properties by the rule of mixtures. The local debonding length for fibers (L_d) is considered 2.5 mm ($L/L_d = 0.12$). The orthotropic four-point bending beam is analyzed for the point loading of 6000 N, with the initial temperature of 320 K, and the temperature increases to 470 K during the heating part.

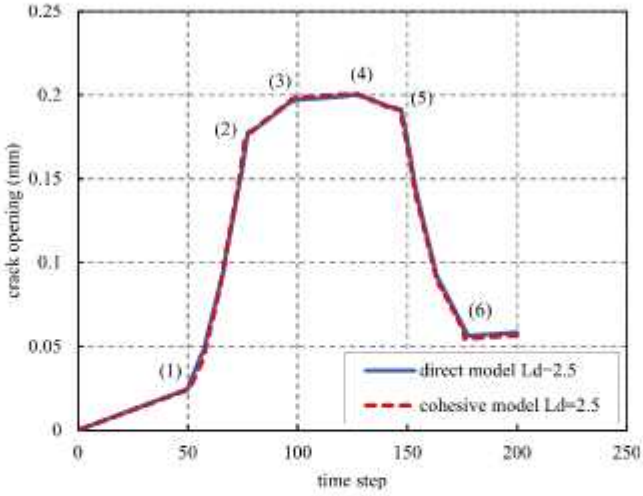

Fig. 12. Crack opening–time step for $L_d = 2.5$ mm.

Fig. 12 depicts the variation of crack opening for the specimen with long fibers tied to the matrix in their length. During the first 100 steps, by increasing the loading, the crack opening increases linearly to reach point (1), and the stress reaches σ_s^M. As a result, the forward phase transformation starts and the opening increases significantly. At point (2), the forward phase transformation is completed. The heating part initiates at point (3), and the opening increases gradually ($T < T_s^A$). During the heating part, the reverse phase transformation of the fibers located near the crack tip starts sooner at point (4). As a result, the opening decreases gradually to reach point (5) in fibers far from the crack tip. Then, the reverse phase transformation initiates for fibers far from the crack tip. It accelerates the crack closure rate, leading to complete reverse phase transformation at point (6). Clearly, the perfect bond analysis shows a good agreement with the direct solution.

The results of the direct model show that the phase transformation of fibers occurs near the crack where the highest crack opening occurs. No phase transformation occurs in other parts.

Fig. 13 illustrates the variations of predicted applied force versus crack opening under the same loading condition for both the isotropic and orthotropic matrices, and for the direct and proposed cohesive models. During the mechanical loading, the crack opening increases by the increase of loading. In the initial linear elastic stage, a small difference exists between the isotropic and orthotropic cases, which is negligible in comparison with the nonlinear phase. Due to different modulus of elasticity, the forward phase transformation in the isotropic case initiates sooner than the orthotropic one and, accordingly, the two cases depart each other after the phase transformation. Later, the results show lower crack opening at the same loading value for the orthotropic case after the forward phase transformation.

The heating of SMA fibers results in the decrease of crack opening up to 70 percent by the increase of temperature, as depicted with the horizontal part in Fig. 13, showing a significant crack closure for both cases.

4.3. Effect of varying fiber volume fraction

To further investigate the self-healing property of SMA composites, various fiber volume fractions are considered for the same four-point bending composite beam and with the same loading condition.

The crack opening is compared for three different volume fractions during the loading and heating processes. Results demonstrate that the composite with lower volume fraction has a greater crack opening at the end of loading part. Moreover, it is observed that the crack opening for each fiber volume fraction remains positive at the end of heating process, which shows that the crack in all simulations is not fully closed due to the presence of external load during the heating process.

Table 6 presents the prediction of crack closure and martensitic volume fraction at the end of loading part for each fiber volume fraction. Both cases of 1% and 1.25% volume fractions show approximately 70% crack closure, while greater volume fractions show lower crack closures.

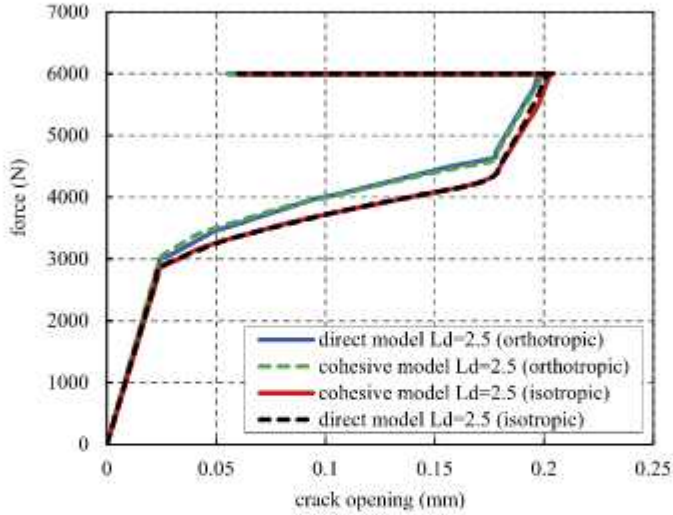

Fig. 13. Force–crack opening for $L_d = 2.5$ mm.

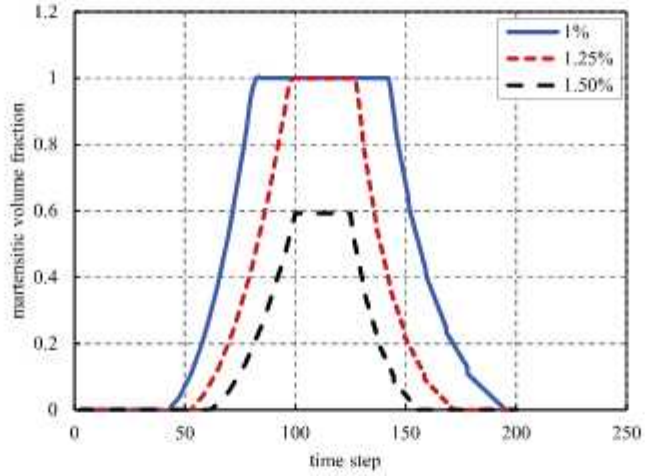

Fig. 14. Variations of the martensitic volume fraction for various fiber fractions.

Table 6
Result of different fiber volume fractions.

Fiber volume fraction (%)	Crack closure present (%)	Martensitic volume fraction at the end of loading part	Crack opening at the end of loading part (mm)	Crack opening at the end of heating part (mm)
1	67.76	1	0.6115	0.1987
1.25	70.33	1	0.5359	0.1667
1.5	61.15	0.593	0.3425	0.1449

Analysis for each fiber volume fraction is performed with the same loading and heating condition. Both cases of 1% and 1.25% volume fractions show complete forward and reverse phase transformations. However, for the 1.5% volume fraction, the forward and reverse phase transformations are not completed, as illustrated in Fig. 14.

Based on the fact that the composite beam with lower fiber volume fraction is more flexible than the same composite beam with higher fiber volume fraction under a specific load, the maximum crack opening of the beam

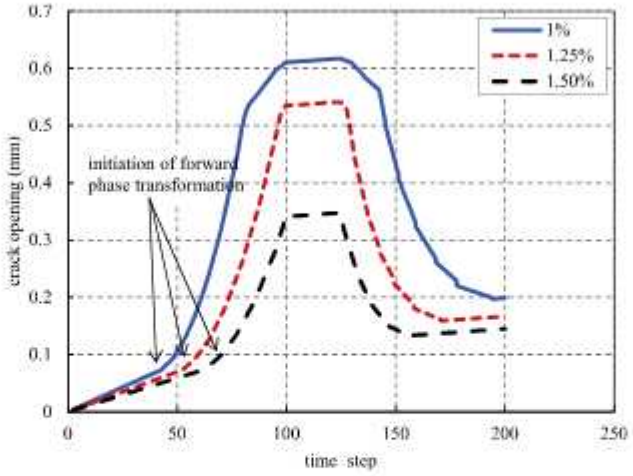

Fig. 15. Variations of the crack opening for various volume fiber fractions.

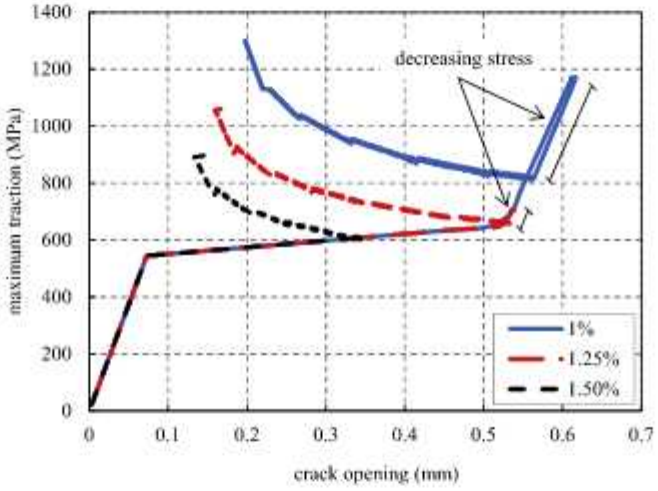

Fig. 16. Maximum traction–crack opening responses for various volume fiber fractions.

with lower fiber volume fraction is greater and the forward phase transformation of fibers initiates sooner, as depicted in Fig. 15.

Fig. 16 demonstrates the traction–crack opening responses for each fiber volume fraction. They show a linear decrease of stress level for 1% and 1.25% fiber volume fractions, as depicted in Fig. 16. This decreasing trend occurs due to the difference in initiation of the reverse transformation in fibers. However, for 1.5% fiber volume fraction, the forward phase transformation is not completed for any of the fibers. Therefore, by increasing the temperature, all fibers initiate the reverse transformation at the same time.

4.4. Tension problem

The same geometry and fiber volume fraction as the four-point bending composite beam is assumed, but the tensile loading condition is considered (Fig. 17). The simulation is repeated for two different local debonding lengths of fibers: 2.5 and 7.5 mm ($L = L_d$). The tensile pre-cracked beam is subjected to a uniform stress loading, which increases to 7000 MPa under the constant temperature of 320 K, while during the heating part, the temperature increases to 470 K.

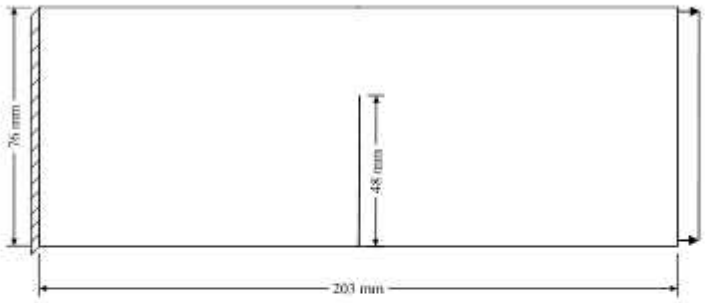

Fig. 17. Tensile cracked beam.

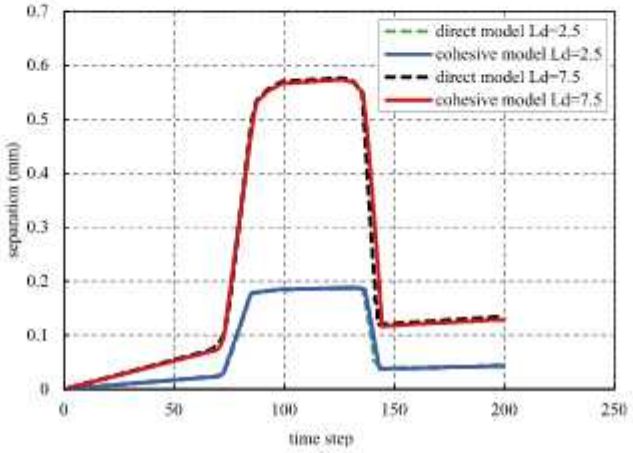

Fig. 18. Crack opening–time step response for various fiber lengths.

Table 7
Material properties of matrix.

Property	Value
Elastic modulus, E (MPa)	5800
Poisson's ratio υ	0.21
Fiber volume fraction %	1

The results, depicted in Fig. 18, exhibit a more linear forward and reverse phase transformation behavior than the bending beam due to simplicity of the loading condition.

Results of simulations under different loading conditions have shown that the adapting cohesive method agrees well with the direct model. In addition, this model overcomes some of the complexities of direct models because it does not require separate modeling of the fibers or direct computation of the stiffness of fibers.

4.5. Crack propagation problem

One of the difficulties in analyzing fiber-reinforced composite problems is the crack propagation. Hence, the developed algorithm is now adopted to investigate a complex mixed-mode fracture propagation problem. The specimen geometry and boundary conditions are illustrated in Fig. 19.

Fibers are distributed in two directions (−45/+45), so the matrix can be assumed isotropic with properties listed in Table 7. The initial crack length is 2 mm, and the local debonding length is considered 5 mm for fibers.

The specimen is simulated under the point load of 1090 N with the initial temperature of 320 K. During the heating part, the temperature further increases to 160 K.

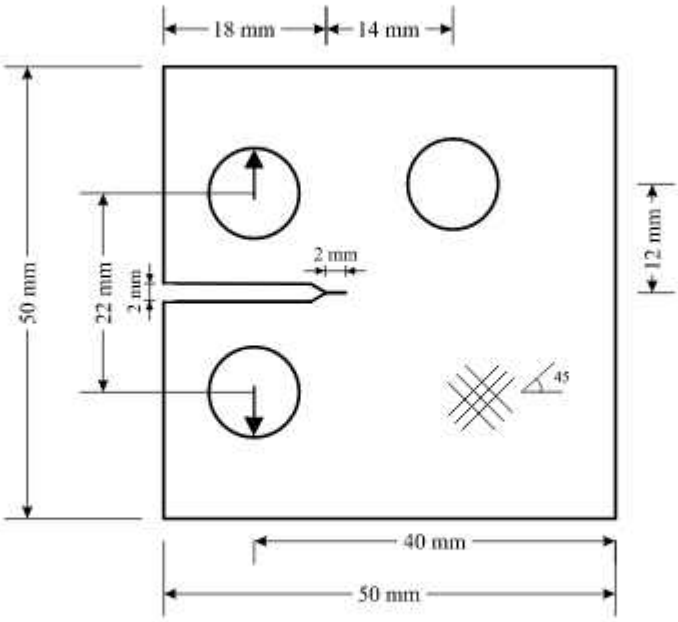

Fig. 19. The mixed-mode specimen (thickness = 10 mm).

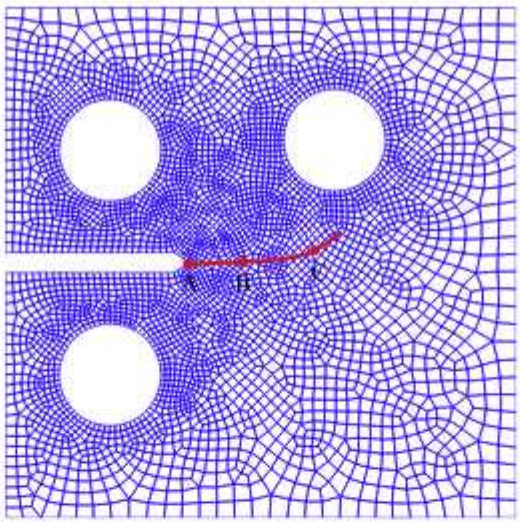

Fig. 20. Crack propagation path.

Since the fibers are distributed in two directions, the developed method determines the crack opening in each direction, and then computes the traction on crack edges. Fig. 20 illustrates the predicted crack propagation path. In the loading part, the crack opening is increased, and when the fracture energy reaches the fracture toughness, the crack starts to propagate. As a result, more fibers bridge the crack. Fibers at different parts of crack gradually begin the forward phase transformation. More fiber bridging leads to the increase of loading capacity until the system reaches a balance at the end of loading part, and the crack propagation stops.

Crack opening results during the loading and heating processes for three points A, B and C, located at $x = -7$, $x = -1$ and $x = 6$, respectively, are presented in Fig. 21. Point A represents the maximum crack opening which is about 0.5 mm. Other points undergo lower openings with maximum values of 0.3 and 0.18 for point B and C, respectively. Crack opening decreases during the heating process due to shape recovery of fibers.

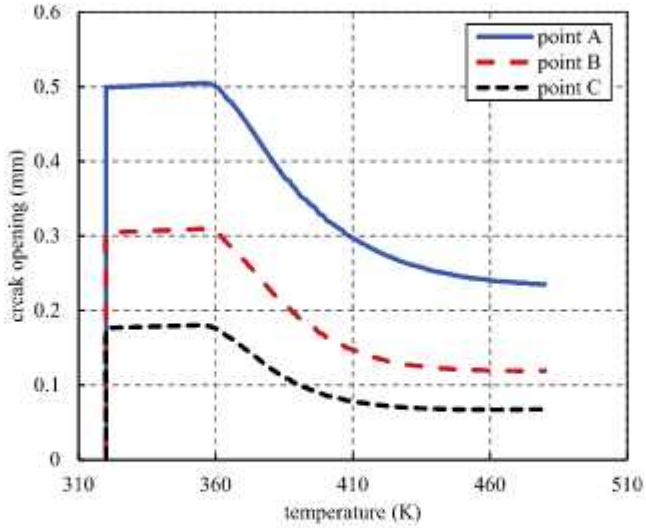

Fig. 21. Crack opening–temperature curves at different points.

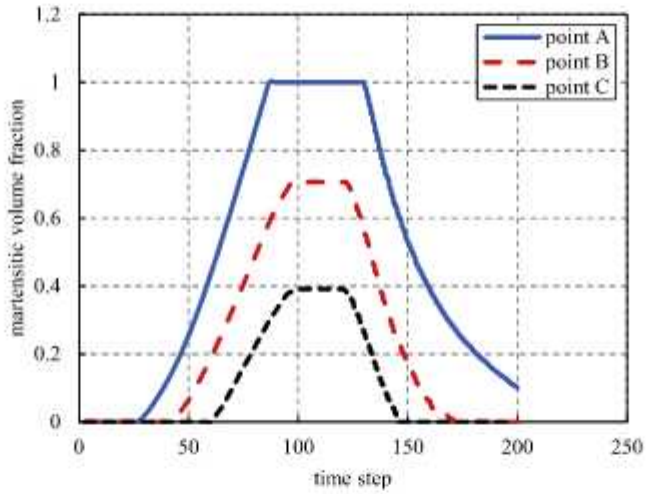

Fig. 22. Variations of the martensitic volume fraction for various fiber fractions.

As illustrated in Fig. 22, point A experiences a complete phase transformation, whereas, in other points on the crack, which undergo lower openings, only a partial phase transformation occurs. For instance, in points B and C, the martensitic volume fractions at the end of loading part are approximately 0.7 and 0.4, respectively. Fig. 22 shows that the reverse phase transformation in point A has not completed due to the presence of external load.

Table 8 compares the crack opening displacements after the loading and heating parts for different points. It demonstrates that points B and C have a greater rate of crack closure than point A. As a result, greater crack closures occur near the crack tip, although it does not exceed 62% in any point of the crack.

Deformed configurations at the end of loading and heating parts are displayed in Fig. 23. It clearly shows how the crack closure occurs after the heating process.

The stress contours at the end of heating and loading parts, depicted in Figs. 24 and 25, demonstrate that the highest stress concentration occurs near the crack tip after the loading part. During the heating process, the reverse fiber transformation to the austenite phase reduces the crack opening. As a result, the stress concentration level decreases near the crack edges and crack tip.

Table 8
Result of crack propagation analysis at different points.

Point	Crack closure (%)	Martensitic volume fraction at the end of loading part	Crack opening at the end of loading part (mm)	Crack opening at the end of heating part (mm)
A	53	1	0.5	0.235
B	61	0.706	0.305	0.119
C	62	0.392	0.177	0.067

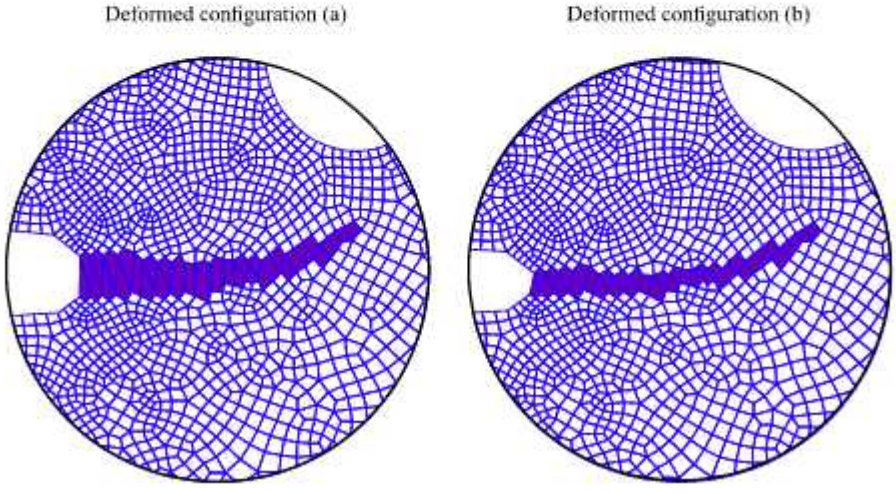

Fig. 23. Predicted deformed configurations near the crack (with magnification factor of 4). (a) After the loading part. (b) After the heating part.

To examine the mesh independency of crack propagation analysis, this problem is now examined with three different meshes, depicted in Fig. 26. Fig. 27 clearly illustrates that the crack propagation path is not sensitive to the adopted finite element mesh. Moreover, these results clearly show that the proposed approach can efficiently model mixed mode crack propagation and healing problems.

5. Conclusion

In this study, a new method has been presented for SMA fiber composite simulation and its self-healing property. A cohesive formulation has been developed to examine the crack behavior and crack healing in SMA composites. Traction on the crack surfaces due to the presence of fibers is simulated with an adapting traction–separation law, with an emphasis on the assumption that the fibers forward phase transformation occurs just near crack edges, with no phase transformation in other areas due to lower strain levels in fibers. A specific length is considered for fibers near the crack edges, to represent the local debonding between fibers and matrix.

Moreover, a direct model has been used for unidirectional fiber composites to validate the main proposed approach. Results of the two models show a good agreement and illustrate that the new proposed cohesive formulation performs well for composites with shorter local debonding lengths.

Furthermore, adapting an extended finite element formulation based on the critical energy criterion has allowed for modeling arbitrary mixed-mode crack propagation and healing in SMA composite problems. The developed cohesive formulation readily allows for analysis of different fiber orientations. The results show that the traction, which exists on the crack surfaces due to the fiber reverse transformation during the heating process, provides sufficient force on the crack faces for crack closure or healing. The amount of crack closure depends on the fiber volume fraction, loading and heating.

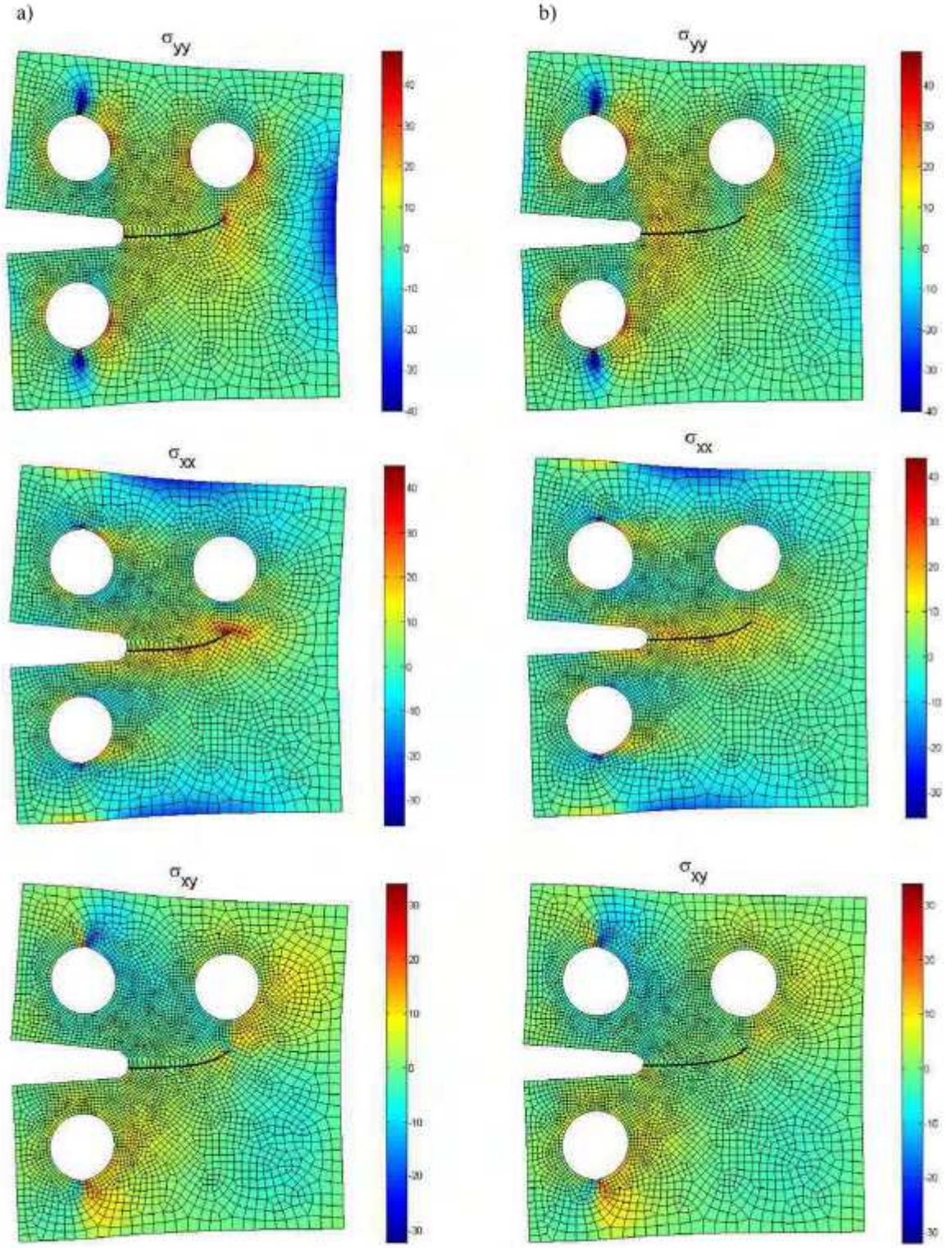

Fig. 24. Stress contours (a) after the loading part, (b) after the heating part.

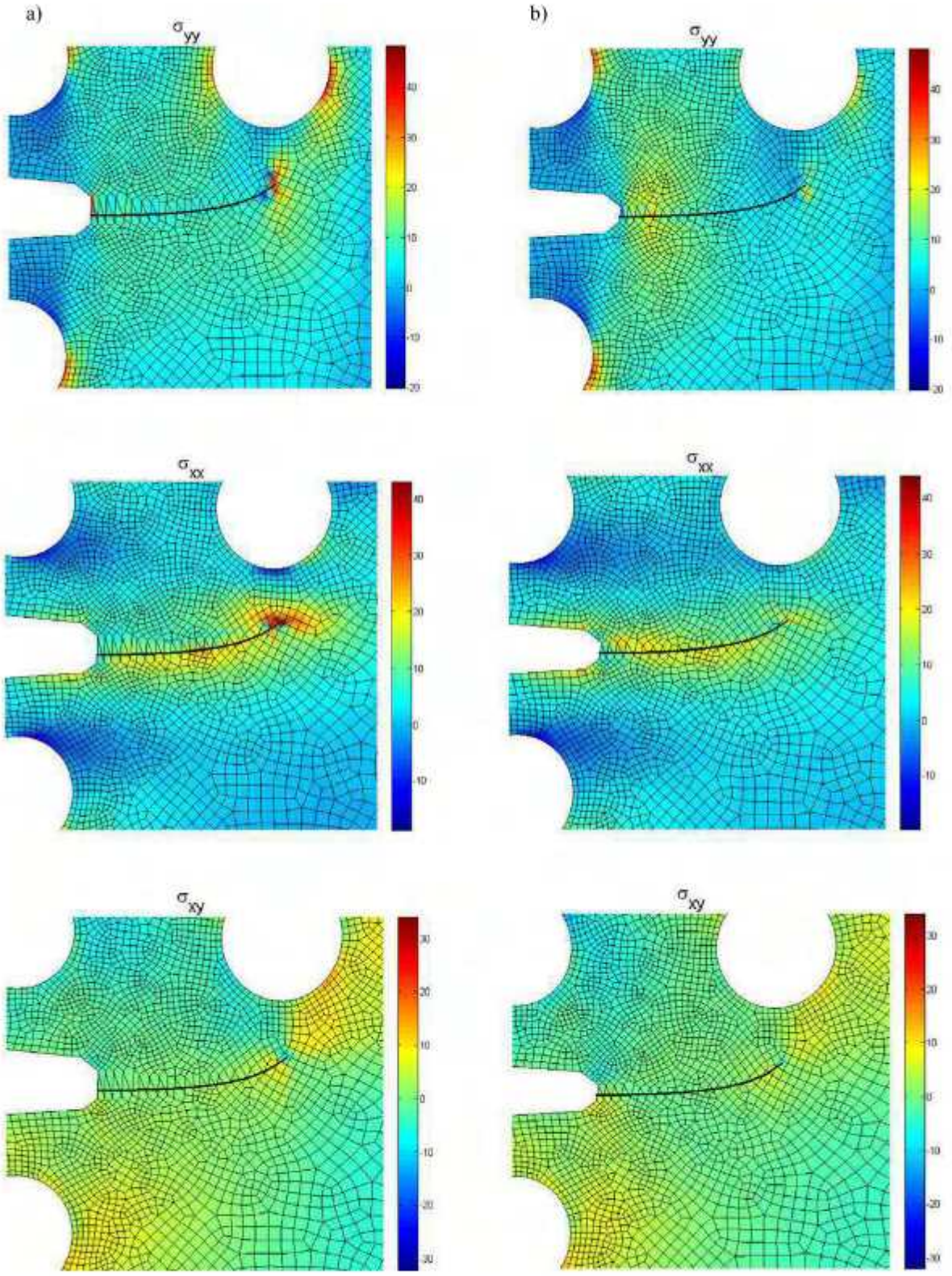

Fig. 25. Stress contours (a) after the loading part, (b) after the heating part.

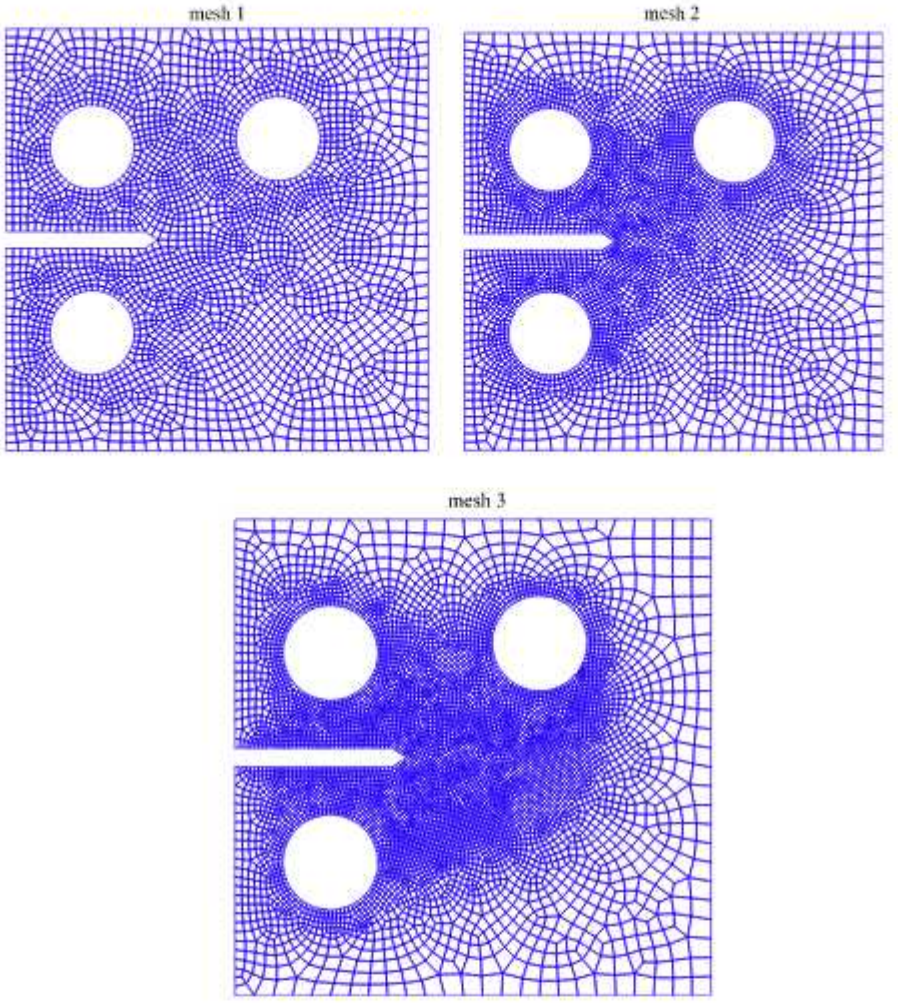

Fig. 26. Sensitivity analysis with three meshes (2730, 3869, 6664 elements, respectively).

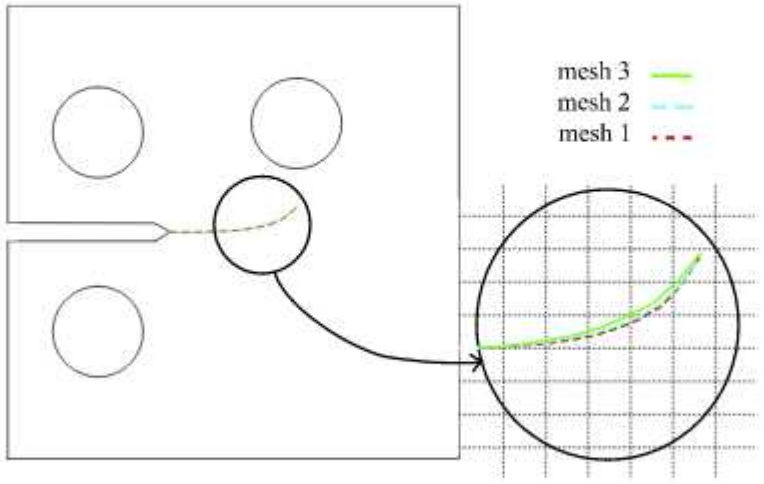

Fig. 27. Crack propagation path for three different meshes.

Acknowledgments

The authors wish to gratefully acknowledge the technical support of the High Performance Computing Lab, School of Civil Engineering, University of Tehran. The financial support of Iran National Science Foundation (INSF) is gratefully acknowledged.

References

[1] J.G. Boyd, D.C. Lagoudas, Thermomechanical response of shape memory composites, J. Intell. Mater. Syst. Struct. 5 (3) (1994) 333–346.
[2] G.Q. Song, Q.P. Sun, M. Cherkaoui, Role of microstructure in the thermomechanical behavior of SMA composites, J. Eng. Mater. Technol. 121 (1) (1999) 86–92.
[3] M. Kawai, H. Ogawa, V. Baburaj, T. Koga, Micromechanical analysis for hysteretic behavior of unidirectional TiNi SMA fiber composites, J. Intell. Mater. Syst. Struct. 10 (1) (1999) 14–28.
[4] D.C. Lagoudas, D. Moorthy, M.A. Qidwai, J.N. Reddy, Modeling of the thermomechanical response of active laminates with SMA strips using the layerwise finite element method, J. Intell. Mater. Syst. Struct. 8 (6) (1997) 476–488.
[5] S. Marfia, E. Sacco, J.N. Reddy, Superelastic and shape memory effects in laminated shape-memory-alloy beams, AIAA J. 41 (1) (2003) 100–109.
[6] M. Bodaghi, A.R. Damanpack, M.M. Aghdam, M. Shakeri, Active shape/stress control of shape memory alloy laminated beams, Composites B 56 (2014) 889–899.
[7] W. Ostachowicz, M. Krawczuk, A. Zak, Natural frequencies of multi-layer composite plate with embedded shape memory alloy wires, J. Intell. Mater. Syst. Struct. 9 (3) (1998) 232–237.
[8] S.S. Sun, G. Sun, F. Han, J.S. Wu, Thermoviscoelastic analysis for a polymeric composite plate with embedded shape memory alloy wires, Compos. Struct. 58 (2) (2002) 295–302.
[9] M.M. Ghomshei, A. Khajepour, N. Tabandeh, K. Behdinan, Finite element modeling of shape memory alloy composite actuators: theory and experiment, J. Intell. Mater. Syst. Struct. 12 (11) (2001) 761–773.
[10] H.J. Lee, J.J. Lee, J.S. Huh, A simulation study on the thermal buckling behavior of laminated composite shells with embedded shape memory alloy (SMA) wires, Compos. Struct. 47 (1) (1999) 463–469.
[11] J.S. Park, J.H. Kim, S.H. Moon, Thermal post-buckling and flutter characteristics of composite plates embedded with shape memory alloy fibers, Composites B 36 (8) (2005) 627–636.
[12] S. Marfia, E. Sacco, Analysis of SMA composite laminates using a multiscale modelling technique, Internat. J. Numer. Methods Engrg. 70 (10) (2007) 1182–1208.
[13] P.F. Dehaghani, S.H. Ardakani, H. Bayesteh, S. Mohammadi, 3D hierarchical multiscale analysis of heterogeneous SMA based materials, Int. J. Solids Struct. 118 (2017) 24–40.
[14] S.M.R. Khalili, M.B. Dehkordi, E. Carrera, A nonlinear finite element model using a unified formulation for dynamic analysis of multilayer composite plate embedded with SMA wires, Compos. Struct. 106 (2013) 635–645.
[15] E. Artioli, S. Marfia, E. Sacco, R.L. Taylor, A nonlinear plate finite element formulation for shape memory alloy applications, Internat. J. Numer. Methods Engrg. 89 (10) (2012) 1249–1271.
[16] H. Asadi, Y. Kiani, M.M. Aghdam, M. Shakeri, Enhanced thermal buckling of laminated composite cylindrical shells with shape memory alloy, J. Compos. Mater. 50 (2) (2016) 243–256.
[17] S.K. Panda, B.N. Singh, Nonlinear finite element analysis of thermal post-buckling vibration of laminated composite shell panel embedded with SMA fiber, Aerosp. Sci. Technol. 29 (1) (2013) 47–57.
[18] A. Shimamoto, J. Nam, T. Oguchi, T. Azakami, Effect of crack closure by shrinkage of embedded shape-memory TiNi fiber epoxy composite under mixed-mode loading, in: ISAEM 2000: 2 nd International Symposium on Designing, Processing and Properties of Advanced Engineering Materials, 2000, pp. 263–268.
[19] K. Hamada, F. Kawano, K. Asaoka, Shape recovery of shape memory alloy fiber embedded resin matrix smart composite after crack repair, Dental Mater. J. 22 (2) (2003) 160–167.
[20] J.B. Ferguson, B.F. Schultz, P.K. Rohatgi, Zinc alloy ZA-8/shape memory alloy self-healing metal matrix composite, Mater. Sci. Eng. A 620 (2015) 85–88.
[21] P.K. Rohatgi, Al-shape memory alloy self-healing metal matrix composite, Mater. Sci. Eng. A 619 (2014) 73–76.
[22] C. Soutis, Fibre reinforced composites in aircraft construction, Prog. Aerosp. Sci. 41 (2) (2005) 143–151.
[23] A. Riccio, C. Di Costanzo, P.Di. Gennaro, A. Sellitto, A. Raimondo, Intra-laminar progressive failure analysis of composite laminates with a large notch damage, Eng. Failure Anal. 73 (2017) 97–112.
[24] A. Riccio, A. Sellitto, S. Saputo, A. Russo, M. Zarrelli, V. Lopresto, Modelling the damage evolution in notched omega stiffened composite panels under compression, Composites B 126 (2017) 60–71.
[25] S. Araki, H. Ono, K. Saito, Micromechanical analysis of crack closure mechanism for intelligent material containing TiNi fibers, JSME Int. J. A 45 (2) (2002) 208–216.
[26] D.S. Burton, X. Gao, L.C. Brinson, Finite element simulation of a self-healing shape memory alloy composite, Mech. Mater. 38 (5) (2006) 525–537.
[27] P. Zhu, Z. Cui, M.S. Kesler, J.A. Newman, M.V. Manuel, M.C. Wright, L.C. Brinson, Characterization and modeling of three-dimensional self-healing shape memory alloy-reinforced metal-matrix composites, Mech. Mater. 103 (2016) 1–10.
[28] S. Mohammadi, XFEM Fracture Analysis of Composites, Wiley, London, 2012.

[29] S. Kumar, I.V. Singh, B.K. Mishra, T. Rabczuk, Modeling and simulation of kinked cracks by virtual node XFEM, Comput. Methods Appl. Mech. Engrg. 283 (2015) 1425–1466.
[30] C. Zhang, C. Wang, T. Lahmer, P. He, T. Rabczuk, A dynamic XFEM formulation for crack identification, Int. J. Mech. Mater. Des. 12 (4) (2016) 427–448.
[31] A. Afshar, S.H. Ardakani, S. Mohammadi, Transient analysis of stationary interface cracks in orthotropic bi-materials using oscillatory crack tip enrichments, Compos. Struct. 142 (2016) 200–214.
[32] A. Daneshyar, S. Mohammadi, Strong tangential discontinuity modeling of shear bands using the extended finite element method, Comput. Mech. 52 (5) (2013) 1023–1038.
[33] P. Areias, T. Belytschko, Two-scale shear band evolution by local partition of unity, Internat. J. Numer. Methods Engrg. 66 (5) (2006) 878–910.
[34] A. Zilian, A. Legay, The enriched space–time finite element method (EST) for simultaneous solution of fluid–structure interaction, Internat. J. Numer. Methods Engrg. 75 (3) (2008) 305–334.
[35] A. Afshar, S.H. Ardakani, S. Hashemi, S. Mohammadi, Numerical analysis of crack tip fields in interface fracture of SMA/elastic bi-materials, Int. J. Fract. 195 (1–2) (2015) 39–52.
[36] T. Belytschko, R. Gracie, On XFEM applications to dislocations and interfaces, Int. J. Plast. 23 (10) (2007) 1721–1738.
[37] G.N. Wells, L.J. Sluys, A new method for modelling cohesive cracks using finite elements, Internat. J. Numer. Methods Engrg. 50 (12) (2001) 2667–2682.
[38] N. Moës, T. Belytschko, Extended finite element method for cohesive crack growth, Eng. Fract. Mech. 69 (7) (2002) 813–833.
[39] G. Nian, Y. Shan, Q. Xu, S. Qu, Q. Yang, Failure analysis of syntactic foams: A computational model with cohesive law and XFEM, Composites B 89 (2016) 18–26.
[40] A. Carpinteri, Post-peak and post-bifurcation analysis of cohesive crack propagation, Eng. Fract. Mech. 32 (2) (1989) 265–278.
[41] P. Bocca, A. Carpinteri, S. Valente, Mixed mode fracture of concrete, Int. J. Solids Struct. 27 (9) (1991) 1139–1153.
[42] T.N. Bittencourt, A.R. Ingraffea, J. Llorca, Simulation of arbitrary, cohesive crack propagation, Fract. Mech. Concr. Struct. 1 (1992) 339–350.
[43] T. Belytschko, N. Moës, S. Usui, C. Parimi, Arbitrary discontinuities in finite elements, Internat. J. Numer. Methods Engrg. 50 (4) (2001) 993–1013.
[44] L. Zhao, J. Zhi, J. Zhang, Z. Liu, N. Hu, XFEM simulation of delamination in composite laminates, Composites A 80 (2016) 61–71.
[45] L. Bouhala, A. Makradi, S. Belouettar, H. Kiefer-Kamal, P. Fréres, Modelling of failure in long fibres reinforced composites by X-FEM and cohesive zone model, Composites B 55 (2013) 352–361.
[46] L. Bouhala, A. Makradi, S. Belouettar, A. Younes, S. Natarajan, An XFEM/CZM based inverse method for identification of composite failure parameters, Comput. Struct. 153 (2015) 91–97.
[47] L. Zhao, Y. Wang, J. Zhang, Y. Gong, N. Hu, N. Li, XFEM-based model for simulating zigzag delamination growth in laminated composites under mode I loading, Compos. Struct. 160 (2017) 1155–1162.
[48] J.G. Boyd, D.C. Lagoudas, A thermodynamical constitutive model for shape memory materials. Part I. The monolithic shape memory alloy, Int. J. Plast. 12 (6) (1996) 805–842.
[49] D.C. Lagoudas (Ed.), Shape Memory Alloys: Modeling and Engineering Applications, Springer Science & Business Media, 2008.
[50] A. Afshar, A. Daneshyar, S. Mohammadi, XFEM analysis of fiber bridging in mixed-mode crack propagation in composites, Compos. Struct. 125 (2015) 314–327.
[51] H. Bayesteh, S. Mohammadi, XFEM fracture analysis of orthotropic functionally graded materials, Composites B 44 (1) (2013) 8–25.